PHYSICS OF FLUIDS **28**, 062004 (2016)

Theoretical study of alignment dynamics of magnetic oblate spheroids in rotating magnetic fields

Mingyang Tan,[1] Han Song,[2] Pallavi Dhagat,[2] Albrecht Jander,[2] and Travis W. Walker[1,a)]
[1]*CBEE, Oregon State University, Corvallis, Oregon 97331, USA*
[2]*EECS, Oregon State University, Corvallis, Oregon 97331, USA*

(Received 1 April 2016; accepted 17 May 2016; published online 3 June 2016)

Magnetic composites containing anisotropic magnetic particles can achieve properties not possible in corresponding bulk or thin films of the magnetic material. In this work, we discuss how planar magnetic anisotropy may be achieved in a composite by aligning disk-shaped particles in an in-plane rotating magnetic field. Previous efforts have reported a simple model of aligning particles in a high-frequency rotating magnetic field. However, no complete analytic solution was proposed. Here, we provide a full analytic solution that describes the alignment dynamics of microdisks in a rotating field that covers the entire frequency range. We also provide simplified solutions at both high-frequency and low-frequency limits through asymptotic expansions for easy implementation into industrial settings. The analytic solution is confirmed by numerical simulation and shows agreement with experiments. *Published by AIP Publishing.* [http://dx.doi.org/10.1063/1.4953009]

I. INTRODUCTION

Anisotropic microscale architectures can provide directionally dependent bulk properties that far exceed the functionality of the native material. These architectures are found in many natural substances, including the prismatic layers of teeth[1] and mollusk shells[2] and the plywood fiber structures in fish scales,[3] insects,[4] and plants.[5] Inspired by the anisotropic architectures of the natural materials, people are committed to developing new materials that contain aligned particles.[6–9] These materials can exhibit enhanced magnetic, mechanical, optical, and diffusive (heat and mass) properties. For example, soft magnetic composites, consisting of magnetic particles embedded in an insulating matrix, have great potential for a variety of breakthrough applications, including magneto-optics,[10] biological tissue scaffolds,[11,12] drug targeting,[13] and high-frequency applications such as microwave absorption, electromagnetic shielding,[14] inductors, and antennae.[15,16]

The anisotropic properties of non-spherical particles like rods and disks allow them to be aligned by an external driving torque that can be generated by several techniques. Examples include optical tweezers, which use a strongly focused beam of light to trap or move particles with sizes ranging from nanometers to micrometers,[17,18] electrorotation, which generates a rotating electric field to rotate elongated metallic particles,[19] and dielectrophoresis, which uses alternating electric field to manipulate and assemble nanowires.[20,21] Compared to these techniques, manipulation of ferromagnetic nano- and micro-particles by using magnetic fields provides a low-cost, efficient, and non-contact method that is easy to implement.[22]

In this study, aligned composites are created by orienting magnetic microdisks. Since the particles have a high-susceptibility plane ($\chi_{\perp}^{E}$) in the radial direction perpendicular to the orientation vector, **p**, and a low-susceptibility axis ($\chi_{\parallel}^{E}$) that is parallel to **p** as shown in Figure 1(a), a planar rotating magnetic field can be used to align the particles in the plane (see Figure 1(b)). This work presents a theoretical model that describes the dynamics associated with the orientation of a magnetic oblate spheroid being aligned by a rotating magnetic field.

a)Electronic mail: travis.walker@oregonstate.edu

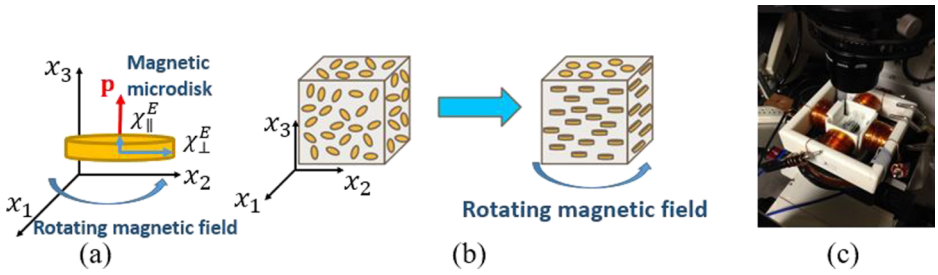

FIG. 1. (a) Magnetic microdisk with in-plane susceptibility, $\chi_{\perp}^{E}$, and out-of-plane susceptibility, $\chi_{\parallel}^{E}$, where $\chi_{\perp}^{E} > \chi_{\parallel}^{E}$, and with orientation vector, **p**. (b) Microdisks aligned by a rotating magnetic field into planar alignment. At first, the microdisks have a random distribution of orientation in the absence of a magnetic field. Upon introducing a rotating magnetic field, the microdisks are aligned such that their $\chi_{\parallel}^{E}$ axis is perpendicular to the magnetic field plane. (c) The setup of the experiment–a three-axis electromagnetic coil system mounted on an inverted microscope. The z-coil (not visible) is underneath the x-y coils seen in the picture.

Kimura *et al*. studied the dynamics of diamagnetic polymer fibers under both static and dynamic magnetic fields.[23,24] Since a diamagnetic fiber has a lower magnetic susceptibility in its long axis than in its radial plane,[25] its magnetic anisotropy is similar to a ferromagnetic disk, even though the geometries differ. Kimura *et al*. provided an analytic model to describe the alignment dynamics of diamagnetic rods in a static magnetic field.[23] They also reported a simple model that describes the alignment dynamics of diamagnetic rods at the high rotating-frequency limit.[24] However, a complete analytic model that covers all possible frequencies is needed to describe the alignment dynamics of oblate spheroids or disks in a rotating field.

In this study, two types of magnetic fields – *constant* and *rotating* – are investigated. These fields can be constructed in a single mathematical representation by designating the constant field to have a rotating frequency of zero. For a microdisk in a constant magnetic field, the low-susceptibility axis $\left(\chi_{\parallel}^{E}\right)$ quickly aligns perpendicular to the field direction in a short time, but the disk still has the freedom to rotate within the plane that is perpendicular to the field direction.

In experiments observing Ni-Fe magnetic microdisks $\left(\chi_{\perp}^{E} > \chi_{\parallel}^{E}\right)$ in a rotating magnetic field, the high-susceptibility plane of the microdisk is found to seek the shortest opportunity to be aligned with the magnetic field, which is the short-term response driven by magnetics.[15,26] While the microdisk is rotating with the magnetic field, it experiences a hydrodynamic drag caused by the fluid. To reduce the drag, the microdisk will find a position where the drag can be minimized. Minimum drag is achieved when the plane of the microdisk is aligned in the plane where the field rotates (i.e., the microdisk reduces the amount of area that the bluff body projects perpendicular to the flow that is caused by the particle's rotation). This drag reduction is the long-term response driven by hydrodynamics, allowing the orientation of magnetic microdisk. If the microdisks can then be frozen in place, a composite with uniformly oriented microdisk fillers can be created as shown in previous work.[15,26] We provide analytic mathematical models that describe the dynamics in both constant and rotating magnetic fields. The analytic models are confirmed by finite difference numerical methods of the governing dynamical systems. Comparisons showing agreement between the models and experiments are also presented. With the knowledge of dynamics of oblate spheroids in fluids, we can fabricate composites with oblate spheroids of different orientations. We can also study the dependence of bulk rheological properties of composites on the orientation of the particles.

II. EXPERIMENTAL METHODS AND MATERIALS

In this study, we will compare our mathematical models to experiments following the work of Song *et al*.[15,26] Ferromagnetic Ni-Fe microdisks with approximately 5 μm diameter and 150 nm thickness (aspect ratio, $\rho \approx 33$) are investigated. The Ni-Fe microdisks are fabricated by wet etching photolithographically patterned permalloy thin films. The microdisks are suspended in a

viscosity-standard silicon oil with viscosities of 215 cp and 550 cp (Brookfield Engineering Laboratories, Inc.), which were measured using a rotational rheometer (DHR-3, TA Instruments). The magnetic field is generated by a three-axis electromagnetic coil system. Initially, an out-of-plane (1,3-plane) field is generated to align microdisks perpendicular to the plane of observation to maximize unalignment (see Figure 1(b)). Then, an in-plane (1,2-plane) field is generated to align the microdisks into the plane of observation. To achieve a rotating magnetic field, the 1 and 2 axis coils are driven in quadrature with cosinusoidal and sinusoidal current via a function generator. The dynamics are observed using a Nikon Ti-S inverted microscope with a 40× objective and recorded by a CCD camera (Guppy Pro 125B, Allied Vision). The setup of the experiment is shown in Figure 1(c).

Ferromagnetic materials, such as the microdisks used in this study, can be magnetized by a magnetic field, forming an induced dipole moment, μ_j. Assuming the induced dipole moment is below saturation (the saturation field is 100 mT for Ni-Fe, and the applied field is below 10 mT), the induced moment scales linearly with external field, particle size, and effective susceptibility such that

$$\mu_j = \frac{V}{\mu_0} \chi^E_{jn} B_n, \tag{1}$$

where μ_j is the induced dipole moment, V is the particle volume, μ_0 is the free space permeability, and B_n is the external magnetic field vector. The effective susceptibility, χ^E_{jn}, is a second-order tensor that relates the particle geometry and the induced dipole moment, describing the degree of magnetization of a material in response to an external field.[27] Generally for ferromagnetic materials, χ^E_{ij} depends on the magnitude of the external magnetic field; however, in the range of working fields in this study (1–10 mT), χ^E_{jn} remains constant for the Ni-Fe microdisk, as determined by vibrating sample magnetometry.

III. MODELING ALIGNMENT DYNAMICS

The goal of this work is to provide a theoretical description of the dynamics of the orientation of microdisks under various external body forces. Here, we derive analytic expressions for the dynamics of oblate spheroids with an induced magnetic dipole in constant and rotating magnetic fields.

Since the aspect ratio of the microdisks used in this study is high, we assume that they can be approximated as oblate spheroids. The microdisks are assumed to be suspended in a quiescent Newtonian fluid. Upon applying a magnetic field, the particles are assumed to have no translational motion, but they are free to rotate. The sedimentation time is at least 15 times as long as the alignment. Thus, the effect of gravity is neglected. The rotating motion of the particle is tracked by the change of the orientation vector, **p** (see Figure 1(a)), a unit vector directed in the axis of symmetry of the particle. Since the particle is axisymmetric, χ^E_{ij} can be decomposed into $\chi^E_{\parallel}$ and $\chi^E_{\perp}$, where $\chi^E_{\parallel}$ is the effective susceptibility parallel to **p**, and $\chi^E_{\perp}$ is the effective susceptibility perpendicular to **p**. Following the work of Kim,[28] the induced dipole moment can be written as

$$\mu_j = \frac{V}{\mu_0} \left(\chi^E_{\parallel} p_j p_n + \chi^E_{\perp} \left(\delta_{jn} - p_j p_n \right) \right) B_n. \tag{2}$$

To model the alignment dynamics of the particles, a torque balance is developed to describe the rotational motion of the particles such that the net torque on the particle is zero, $\sum_k T_i^{(k)} = 0$. In our model, we will initially include three possible torques: T_i^M is the magnetic torque that results from the interaction of the external field and the corresponding induced dipole moment; T_i^H is the hydrodynamic torque that is created by the drag around the particles by the fluid; and T_i^B is the Brownian torque that is caused by thermal fluctuations of fluid molecules around the particles. Since the particle Reynolds number is assumed to be very small, $Re_p \sim O[10^{-7}]$ for our experiments, resulting from the small particle size and slow motion, the use of Stokes flow is valid to model the hydrodynamic torque. The torques are modeled such that[28]

$$T_i^M = \varepsilon_{ijk}\mu_j B_k, \tag{3}$$

$$T_i^H = C_{ij}\left(\Omega_j^\infty - \omega_j\right) + H_{ijk}E_{jk}^\infty, \text{ and} \tag{4}$$

$$T_i^B = -\varepsilon_{ijk}p_j\frac{\partial\left[k_B T\log\Psi\right]}{\partial p_k}, \tag{5}$$

where k_B is the Boltzmann constant, T is the absolute temperature, and Ψ is the probability density distribution of the particles orientation.[28] In Stokes flow, the linearity of the Stokes equations leads to a set of linear relations between moments and flow parameters, where the resistance tensors, C_{ij} and H_{ijk}, relate the hydrodynamic torque to the particle motion.[29] However, since microdisks are assumed to be suspended in a quiescent fluid, the angular velocity, Ω_j^∞, and the rate of strain, E_{jk}^∞, of fluid far from the microdisks are null. Thus, the torque balance provides the following expression for angular velocity of the particle, ω_j, as

$$C_{ij}\omega_j = \varepsilon_{ijk}\mu_j B_k - \varepsilon_{ijk}p_j\frac{\partial\left[k_B T\log\Psi\right]}{\partial p_k}. \tag{6}$$

To model the dynamics of the spheroid during the alignment, the orientation vector is tracked by solving the differential rate of change, such that

$$\frac{dp_i}{dt} = \varepsilon_{ijk}\omega_j p_k, \tag{7}$$

where t is time. If the angular velocity can be written explicitly, a direct substitution into Eq. (7) provides a complete derivation of the particle alignment dynamics. For an axisymmetric particle, the resistance tensor, C_{ij}, can be written as

$$C_{ij} = 8\pi\eta a^3\left(X^C p_i p_j + Y^C\left(\delta_{ij} - p_i p_j\right)\right), \tag{8}$$

where η is fluid viscosity; X^C and Y^C are scalar resistances, which are functions of particle aspect ratio; and a is one-half of the principal axis of the particle.[29] Since an axisymmetric particle is isotropic with respect to the rotation about its center,[30] C_{ij} can be written as $C_{ij} = \zeta_r\delta_{ij}$ such that $\zeta_r = 8\pi\eta a^3 Y^C$ (see proof and details in Appendix A). By substituting the expressions for ω_j, C_{ij}, and μ_j into Eq. (7) and by neglecting the Brownian term, since the Peclét number for the experimental conditions considered here is large (see details in Appendix B), the governing equation is given by

$$\frac{dp_i}{dt} = -\frac{V\left(\chi_\perp^E - \chi_\parallel^E\right)}{\mu_0\zeta_r}B_n p_n\left(B_i - B_k p_k p_i\right). \tag{9}$$

The leading term on the right-hand side contains all of the information regarding the particle and the medium. Since the parameters are held constant for any specific experiment, we define the following combined parameter:

$$A \equiv \frac{V\left(\chi_\perp^E - \chi_\parallel^E\right)}{\mu_0\zeta_r}. \tag{10}$$

For the magnetic microdisks used in this work, the susceptibility in-plane is greater than that out-of-plane $\left(\chi_\perp^E > \chi_\parallel^E\right)$. We can now decouple the magnetic field by setting $B_k \equiv Bb_k$, where B is the magnitude of the magnetic field, and b_k is a unit vector pointing in the direction of the magnetic field. At this point in the derivation, the only time scale that is present is $\left[AB^2\right]^{-1}$, which is the intrinsic time that the particle can be aligned in a specific experiment. Thus, the dimensionless time τ can be defined such that

$$\tau = AB^2 t. \tag{11}$$

The dimensionless governing equation is then given by

$$\frac{dp_i}{d\tau} = -b_n p_n\left(b_i - b_k p_k p_i\right). \tag{12}$$

We can now solve this set of nonlinear ordinary differential equations for various magnitudes of the frequency of the rotating magnetic field. For a dynamic field rotating in the 1, 2-plane, the field direction vector, b_i, is given by

$$b_i = \delta_{i1}\cos\omega t + \delta_{i2}\sin\omega t, \tag{13}$$

where ω is the rotating frequency in radians.

A. Constant field solution

A constant magnetic field is the special case of a rotating field where the frequency of rotation is null ($\omega = 0$); thus, the direction of b_i is constant, and $b_i = \delta_{i1}$ is chosen for convenience. Therefore, Eq. (12) becomes

$$\frac{dp_i}{d\tau} = p_1 p_1 p_i - p_1 \delta_{i1}. \tag{14}$$

Since $\mathbf{p}$ is restricted to the surface of a unit sphere, rewriting the equation in spherical coordinates, where $\mathbf{p} = (\sin\theta\cos\phi, \sin\theta\sin\phi, \cos\theta)$, reduces the number of differential equations. Thus, Eq. (14) then becomes

$$\frac{d\phi}{d\tau} = \frac{1}{2}\sin 2\phi, \text{ and} \tag{15}$$

$$\frac{d\theta}{d\tau} = -\frac{1}{2}\sin 2\theta\cos^2\phi. \tag{16}$$

Eqs. (15) and (16) can be solved analytically, such that

$$\frac{\tan\phi}{\tan\phi_0} = \exp[\tau] \text{ and} \tag{17}$$

$$\frac{\tan\theta}{\tan\theta_0} = \sqrt{\frac{\tan^2\phi_0 + \exp[-2\tau]}{1+\tan^2\phi_0}}, \tag{18}$$

where $\tan\phi_0 = \left.\frac{p_2}{p_1}\right|_{\tau=0}$ and $\tan\theta_0 = \left.\frac{\sqrt{1-p_3 p_3}}{p_3}\right|_{\tau=0}$ are expressions for the initial orientation conditions of the spheroid; and ϕ_0 and θ_0 are the initial azimuthal angle and polar angle respectively. The solution can also be represented in terms of the components of the orientation vector p_i as

$$p_1 = \sqrt{\frac{1}{1+\bar{p}^2\exp[2\tau]}}, \text{ and} \tag{19}$$

$$\sqrt{p_2 p_2 + p_3 p_3} = \frac{\bar{p}}{\sqrt{\bar{p}^2 + \exp[-2\tau]}}, \tag{20}$$

where $\bar{p}^2 = \left.\frac{1-p_1 p_1}{p_1 p_1}\right|_{\tau=0}$ is the initial orientation of the particle. The solution in Eq. (19) indicates that as $\tau \to \infty$, p_1 would vanish (see Figure 2). However, the steady-state values of p_2 and p_3 depend on the initial value, which means that the low-susceptibility axis of the particle is free to rotate within the plane that is perpendicular to the field direction. Thus, we call this situation one-dimensional alignment, since only one major axis of the oblate spheroid is aligned with the magnetic field.

B. Rotating field solution

Now, we turn our focus to the problem where the frequency is not zero. In this case, a dimensionless frequency, ξ, can be defined using the intrinsic time scale as

$$\xi = \frac{2\omega}{AB^2}. \tag{21}$$

The dimensionless frequency can also be called "rotational" Mason number,[31] which is the ratio between magnetic and viscous torques. Here, the factor of 2 is chosen in the dimensionless frequency

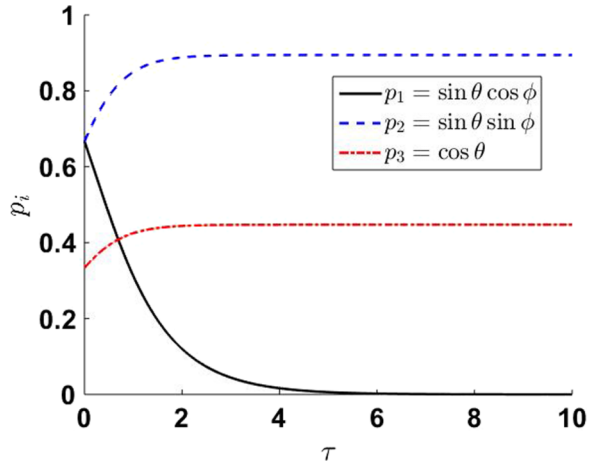

FIG. 2. Evolution of p_1, p_2, and p_3 in constant field. The initial value for $\mathbf{p}$ is set to be $\left(\frac{2}{3}, \frac{2}{3}, \frac{1}{3}\right)$. Thus, p_1 goes to zero regardless of its initial value, since the field is pointing to the direction of 1. The steady-state values of p_2 and p_3 depend on the initial values.

for algebraic convenience, which is a result of the symmetry of the disk. The disk "sees" the field rotate twice as fast, since the disk cannot distinguish the north pole from the south pole of the field direction. Again, writing $\mathbf{p}$ in terms of spherical coordinates and rewriting Eq. (12) in terms of θ and ϕ yields

$$\frac{d\phi}{d\tau} = \frac{1}{2}\sin\left[2\phi - \xi\tau\right] \text{ and} \tag{22}$$

$$\frac{d\theta}{d\tau} = -\frac{1}{2}\sin 2\theta\cos^2\left[\phi - \frac{\xi\tau}{2}\right], \tag{23}$$

which reduce to Eqs. (15) and (16) when $\xi \to 0$. To ease issues with the oscillatory nature of the problem, we define a new variable u, which is defined to be the angle between the magnetic field direction and the projection of the orientation vector $\mathbf{p}$ on the 1, 2-plane, such that

$$u = \phi - \frac{\xi\tau}{2}. \tag{24}$$

Thus, by shifting the frame of reference to the direction of the magnetic field, Eqs. (22) and (23) become

$$\frac{du}{d\tau} = \frac{1}{2}\sin 2u - \frac{\xi}{2} \text{ and} \tag{25}$$

$$\frac{d\theta}{d\tau} = -\frac{1}{2}\sin 2\theta\cos^2 u. \tag{26}$$

This fully nondimensionalized set of first-order, nonlinear ordinary differential equations can be solved as a function of the one governing parameter, ξ, and the corresponding initial conditions, u_0 and θ_0.

1. Full analytic solution

The full analytic solution to Eqs. (25) and (26) is given for three cases of ξ. Detailed derivations are provided in Appendix C.

a. Case $\xi < 1$. If $\xi < 1$, the observed field frequency, 2ω, is smaller than the intrinsic frequency, AB^2, which can be achieved either by making the field rotate slowly or by increasing the field strength. The solution to Eqs. (25) and (26) for $\xi < 1$ is

$$\log\left[\frac{\tan\theta}{\tan\theta_0}\right] = -\frac{\tau}{2} + \frac{1}{2}\log\left[\frac{\sinh^2\Pi}{\sinh^2\Pi_0}\left(\frac{\xi^2 + \left[\sqrt{1-\xi^2}\coth\Pi + 1\right]^2}{\xi^2 + \left[\sqrt{1-\xi^2}\coth\Pi_0 + 1\right]^2}\right)\right], \tag{27}$$

where

$$\Pi = \frac{1}{2}\log\left[\frac{-\xi\tan u + 1 - \sqrt{1-\xi^2}}{-\xi\tan u + 1 + \sqrt{1-\xi^2}}\right], \tag{28}$$

$$\Pi_0 = \frac{1}{2}\log\left[\frac{-\xi\tan u_0 + 1 - \sqrt{1-\xi^2}}{-\xi\tan u_0 + 1 + \sqrt{1-\xi^2}}\right], \text{ and} \tag{29}$$

$$\Pi = \frac{\sqrt{1-\xi^2}}{2}\tau + \Pi_0. \tag{30}$$

The change of the orientation vector, **p**, is shown in Figure 3 for $\xi = 0.5$ with an initial orientation of $\phi_0 = \frac{\pi}{4}$, $\cos\theta_0 = 1 \times 10^{-4}$. Figure 3(a), showing the top view along the 3-direction which is perpendicular to the plane of the rotating field, plots the trajectory of the orientation vector, showing that p_1 and p_2 slowly vanish. Figures 3(b) and 3(c) plot the side view (along the 1- and 2-directions, respectively) of the trajectory, showing that p_3 limits to unity while p_1 and p_2 vanishes. Figure 3(d) plots the change of p_3 with respect to time τ, showing that p_3 goes to unit at steady-state, implying that the particle is aligned.

b. Case $\xi = 1$. If $\xi = 1$, the observed field frequency, 2ω, is equal to the intrinsic frequency, AB^2. The solution to Eqs. (25) and (26) for $\xi = 1$ is

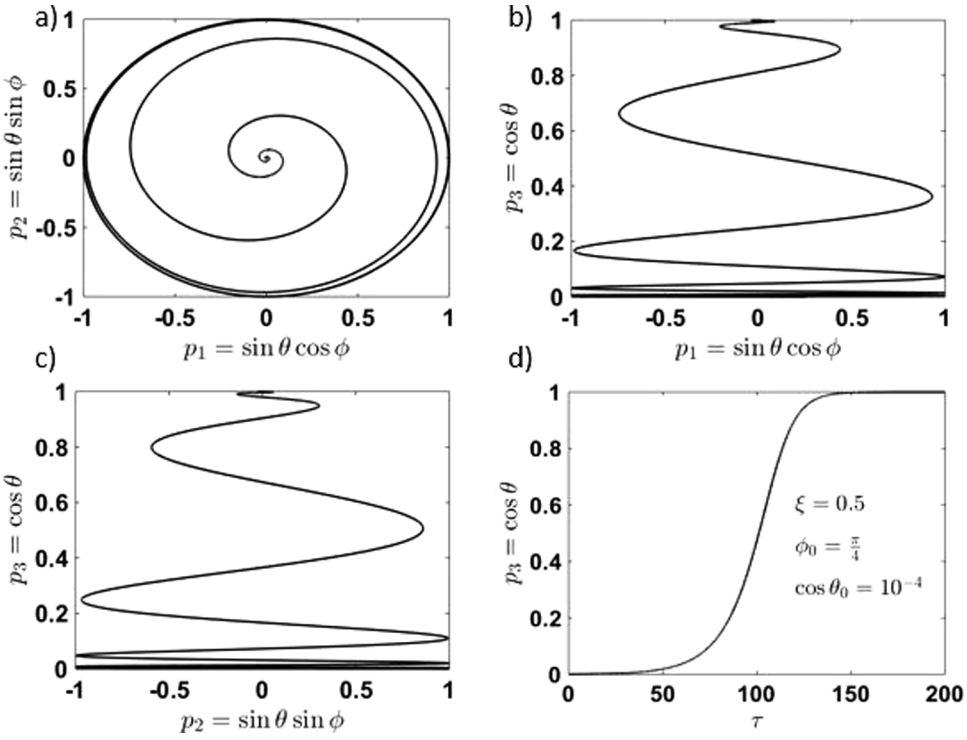

FIG. 3. Evolution of orientation vector **p** at $\xi = 0.5$. (a) View perpendicular to the rotating field. The spiral trajectory shows that p_1 and p_2 slowly limit to 0. (b) and (c) View parallel to the rotating field. At steady state, both p_1 and p_2 vanish, and p_3 limits to 1. (d) Change of p_3 with respect to τ. In long time p_3 slowly limits to 1.

$$\log\left[\frac{\tan\theta}{\tan\theta_0}\right] = -\frac{\tau}{2} + \frac{1}{2}\log\left[\frac{2\Lambda^2 + 2\Lambda + 1}{2\Lambda_0^2 + 2\Lambda_0 + 1}\right], \tag{31}$$

where

$$\Lambda = \frac{1}{\cot u - 1}, \tag{32}$$

$$\Lambda_0 = \frac{1}{\cot u_0 - 1}, \text{ and} \tag{33}$$

$$\Lambda = -\frac{\tau}{2} + \Lambda_0. \tag{34}$$

The $\xi = 1$ case occurs only when the observed field frequency is identical to the intrinsic frequency, making it an unstable case.

c. Case $\xi > 1$. If $\xi > 1$, the observed field frequency, 2ω, is larger than the intrinsic frequency, AB^2, which can be obtained either by making the field rotate faster than that the particle can respond to the field or by decreasing the field strength B. The solution to Eqs. (25) and (26) for $\xi > 1$ is

$$\log\left[\frac{\tan\theta}{\tan\theta_0}\right] = -\frac{\tau}{2} + \frac{1}{2}\log\left[\frac{\cos^2 K}{\cos^2 K_0}\left(\frac{\xi^2 + \left[\sqrt{\xi^2-1}\tan K - 1\right]^2}{\xi^2 + \left[\sqrt{\xi^2-1}\tan K_0 - 1\right]^2}\right)\right], \tag{35}$$

where

$$K = \arctan\left[\frac{1 - \xi\tan u}{\sqrt{\xi^2 - 1}}\right], \tag{36}$$

$$K_0 = \arctan\left[\frac{1 - \xi\tan u_0}{\sqrt{\xi^2 - 1}}\right], \text{ and} \tag{37}$$

$$K = \frac{\sqrt{\xi^2 - 1}}{2}\tau + K_0. \tag{38}$$

The change of the orientation vector, **p**, is shown in Figure 4 for $\xi = 2$ with an initial orientation of $\phi_0 = \frac{\pi}{4}, \cos\theta_0 = 1 \times 10^{-4}$. At $\xi = 2$, the field rotates faster than the particle is able to respond. Thus, the particle appears to "wobble" in response to the rotating field, and the trajectories of p_1 and p_2 are not smooth, creating velocities that appear discontinuous in Figures 4(a)-4(c) and plateaus in Figure 4(d). These characteristics are in direct contrast to the trajectories seen in Figure 3; however, the overall trend of p_3 in both cases is monotonically limiting to unity.

In each of the three cases, the values of u and θ are calculated using the initial value of the azimuthal angle, u_0 (which is equal to ϕ_0). For the case of $\xi < 1$, u_0 is substituted into Eq. (29) to calculate Π_0. Then, at a given time τ, the value of Π can be found by using Eq. (30). With the knowledge of Π, at any given time, the value of θ can be found by Eq. (27). The value of azimuthal angle u (or ϕ via Eq. (24)) can also be found by solving Eq. (28). Similar processes can be followed to find u and θ for the cases $\xi = 1$ and $\xi > 1$.

To enable comparisons to experiments, an alignment time, $\Delta\tau$, is chosen arbitrarily to be the difference in times as the particle aligns from a starting orientation $p_3^{(1)}$ to a final orientation $p_3^{(2)}$, where the alignment is considered to be complete, such that

$$\Delta\tau = \tau\left(p_3^{(2)}\right) - \tau\left(p_3^{(1)}\right). \tag{39}$$

In this work, $p_3^{(1)}$ is chosen to be 0.1, and $p_3^{(2)}$ is chosen to be 0.9. A cartoon representation of this alignment time can be seen in Figure 5. In Figure 6, the alignment time is plotted as a function of dimensionless frequency, ξ. At low ξ, $\xi \ll 1$, $\Delta\tau$ appears to scale as ξ^{-2}, which is validated by the asymptotic expansion on $\xi < 1$ analytic solution in Sec. III B 2 a. At high ξ, $\xi \gg 1$, $\Delta\tau$ is appears to be constant, which is also shown in the asymptotic solution to Eqs. (25) and (26) in Sec. III B 2 b.

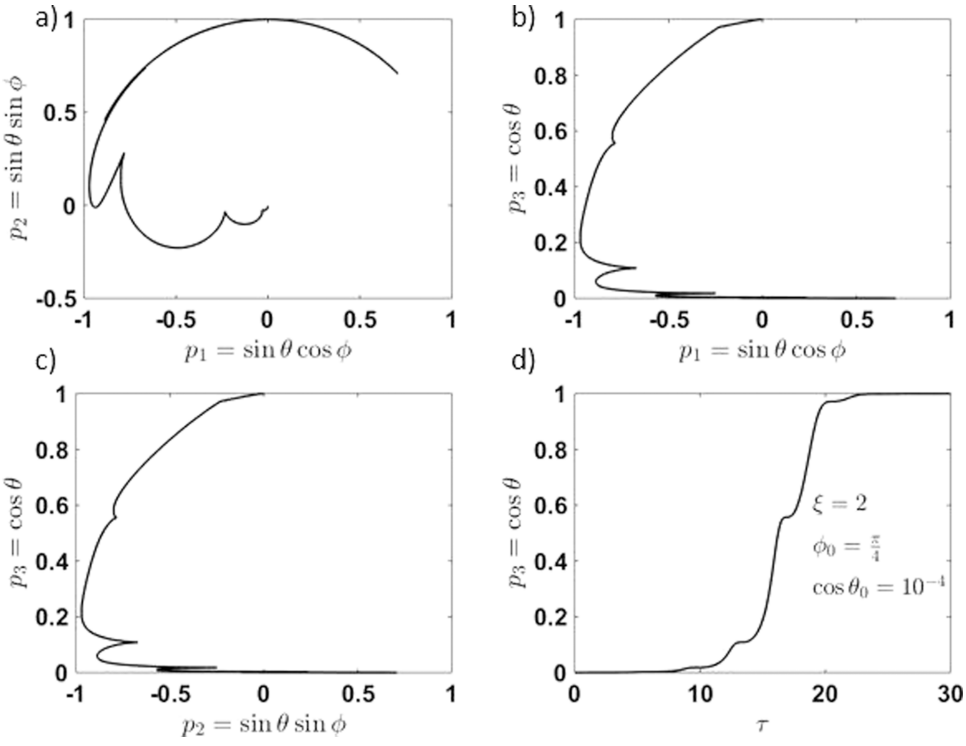

FIG. 4. Evolution of orientation vector **p** at $\xi = 2$. (a) View perpendicular to the rotating field. The shorter trajectory shows that p_1 and p_2 rapidly limit to 0. (b) and (c) View parallel to the rotating field. At steady state, both p_1 and p_2 vanish, and p_3 limits to 1. (d) Change of p_3 with respect to τ. In long time p_3 rapidly limits to 1.

2. Asymptotic solutions

Though complete, the solutions derived in Sec. III B 1 are cumbersome to implement, disguising the simplicity of the effect of ξ on the alignment time. Simplified expressions would be more manageable for implementation into industrial settings. Thus, in an attempt to make the solutions more tractable, asymptotic expressions are derived for the two limiting cases of ξ visualized in Figure 6.

a. Case $\xi \ll 1$ ($\xi \to 0$). Eq. (27), the full solution for $\xi < 1$, can be rewritten in terms of exponentials to ease the asymptotics, such that

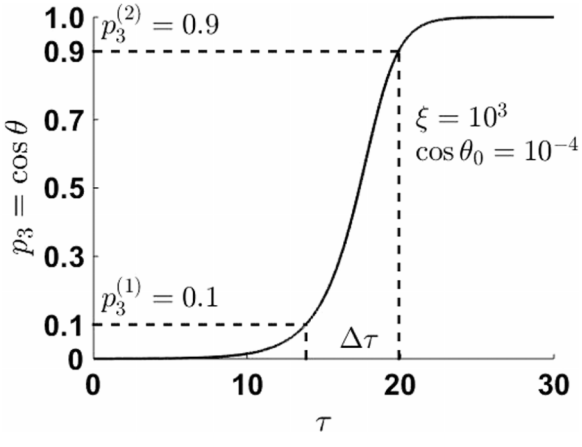

FIG. 5. The alignment time, $\Delta\tau$, is chosen to be time from $p_3^{(1)} = 0.1$ to $p_3^{(2)} = 0.9$.

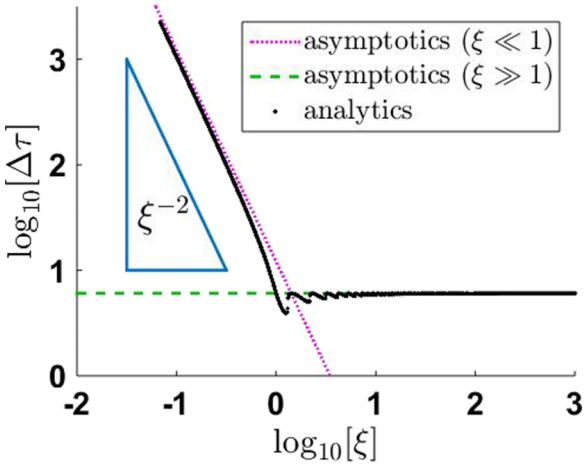

FIG. 6. The alignment time, $\Delta\tau$, chosen from $p_3 = 0.1$ to $p_3 = 0.9$ versus ξ from both analytics and asymptotics. Asymptotic expansions show that $\Delta\tau$ scales as ξ^{-2} at $\xi \ll 1$ and $\Delta\tau$ scales as ξ^0 at $\xi \gg 1$.

$$\frac{\tan\theta}{\tan\theta_0} = [\Gamma_1 + \Gamma_2 + \Gamma_3]^{1/2}, \tag{40}$$

where

$$\Gamma_1 = \left(\frac{\lambda_2 + \lambda_0 - 2\xi\lambda_1}{1-\xi^2} + \frac{\lambda_2 - \lambda_0}{\sqrt{1-\xi^2}}\right)\frac{\exp\left[-\tau(1-\sqrt{1-\xi^2})\right]}{2}, \tag{41}$$

$$\Gamma_2 = \left(\frac{\lambda_2 + \lambda_0 - 2\xi\lambda_1}{1-\xi^2} + \frac{\lambda_0 - \lambda_2}{\sqrt{1-\xi^2}}\right)\frac{\exp\left[-\tau(1+\sqrt{1-\xi^2})\right]}{2}, \text{ and} \tag{42}$$

$$\Gamma_3 = \left(2\lambda_1\frac{\xi}{1-\xi^2} - \frac{\xi^2}{1-\xi^2}\right)\exp\left[-\tau\right], \tag{43}$$

such that

$$\lambda_0 = \frac{1}{1+\tan^2\phi_0}, \tag{44}$$

$$\lambda_1 = \frac{\tan\phi_0}{1+\tan^2\phi_0}, \text{ and} \tag{45}$$

$$\lambda_2 = \frac{\tan^2\phi_0}{1+\tan^2\phi_0}. \tag{46}$$

As $\xi \to 0$, Γ_2 and Γ_3 decay much faster than Γ_1, and at long time, $\Gamma_1 \gg \Gamma_2, \Gamma_3$. Thus, the leading-order Taylor expansions of each of the Γ-terms results in the following simplification for Eq. (40) (details provided in Appendix D), where

$$\frac{\tan\theta}{\tan\theta_0} = \left[\lambda_2 \exp\left[-\frac{\xi^2\tau}{2}\right]\right]^{1/2}. \tag{47}$$

The alignment time in Eq. (39) can be simplified to

$$\Delta\tau = \frac{-2}{\xi^2}\log\left[\frac{\tan^2\theta_2}{\tan^2\theta_1}\right], \tag{48}$$

where $\theta_2 = \cos^{-1} p_3^{(2)}$ and $\theta_1 = \cos^{-1} p_3^{(1)}$. The alignment time scales with ξ^{-2} at low ξ. Further, by taking the limit of Eq. (40) as $\xi \to 0$, the constant field solutions in Eqs. (17) and (18) are recovered, confirming the low-ξ asymptotic solution.

b. Case $\xi \gg 1$ ($\xi \to \infty$). If the magnetic field rotates much faster than the particle can respond ($\xi \gg 1$), the long-term response dominates. Starting with Eq. (25),

$$\frac{du}{d\tau} \approx -\frac{\xi}{2}, \tag{49}$$

since $\xi \gg \sin 2u$. This equation can be solved easily such that

$$u = \phi_0 - \frac{\xi}{2}, \tag{50}$$

where ϕ_0 (the initial azimuthal angle) is equal to u_0 (the initial phase shift) by Eq. (24). Also, from Eq. (24), the expression

$$\phi = \phi_0 \tag{51}$$

is a straightforward result, which means, at high ξ, the azimuthal angle does not change. Substituting Eq. (50) into Eq. (26) gives the following differential equation for the alignment:

$$\frac{d\theta}{d\tau} = -\frac{1}{2}\sin 2\theta \cos^2\left[\phi_0 - \frac{\xi\tau}{2}\right]. \tag{52}$$

Separating and integrating this expression gives

$$\frac{\tan\theta}{\tan\theta_0} = \exp\left[-\frac{\tau}{2} + \frac{\phi_0}{\xi} + \frac{\sin\left[2\phi_0 - \xi\tau\right]}{\xi}\right], \tag{53}$$

which can be further simplified by assuming $\xi \to \infty$, such that

$$\frac{\tan\theta}{\tan\theta_0} = \exp\left[-\frac{\tau}{2}\right]. \tag{54}$$

The solution in Eq. (54), derived rigorously here, is consistent with the work of Kimura.[24]

IV. RESULTS AND DISCUSSION

In the constant-field solution, if we shift the dimensionless time by a factor of $(-\log \bar{p})$, Eq. (19) becomes

$$p_1 = \sqrt{\frac{1}{1 + \exp\left[2\tau\right]}}, \tag{55}$$

which is independent of the initial value of p_1. This result indicates that the particle follows the same alignment path for any initial condition, which is consistent with general Stokes flow principles.

For $\xi < 1$, separate short-term and long-term responses are noticeable, resulting from motion that is initially either in the azimuthal ϕ-direction or in the polar θ-direction, depending on the value of ϕ_0 and θ_0. If $\theta_0 < \frac{\pi}{2} - \phi_0$, the shortest path to alignment is in the θ-direction, and a separate short-term response is seen as a quick θ-motion, as visualized in trajectories for $\phi_0 = 0$ and $\phi_0 = \frac{\pi}{4}$ in Figure 7. After the major axis of spheroid is locked into position with the field, the long-term response proceeds to align the easy plane over a significantly longer time. If $\theta_0 > \frac{\pi}{2} - \phi_0$, the short-term response will be in the azimuthal ϕ-direction, and no quick alignment motion will be observed (viz. the $\left(\phi_0 = \frac{\pi}{2}\right)$-case in Figure 7).

For $\xi > 1$, the field rotates so fast that it can be approximated as a planar field, and only the long-term hydrodynamic response will be present. As derived in Eq. (54), the evolution of p_3 becomes independent of ξ and ϕ_0 as ξ grows large, as visualized in Figure 8, where the solutions collapse into a single trajectory. In Figure 8, when $\xi = 10$, the particle "wobbles," as previously discussed, while it attempts to move with the field. When $\xi = 10^3$, the field rotates so fast that the particle experiences the effects of the field in all directions, making the major axis always aligned regardless of ϕ_0.

To validate theory, we compare single particle experiments at varying ξ to the models. The experiments show that the alignment time is constant at high ξ. At low ξ, where we predict that

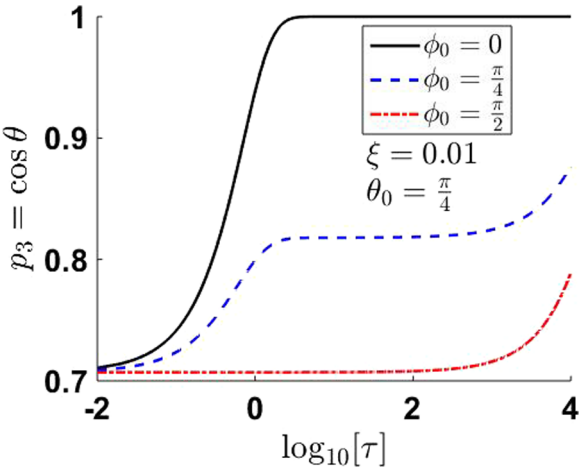

FIG. 7. The evolution of p_3 at $\xi = 0.01$ with $\theta_0 = \frac{\pi}{4}$ for $\phi_0 \in \{0, \frac{\pi}{4}, \frac{\pi}{2}\}$. A short-term response of θ-motion can be observed for the $\phi_0 = 0$ and $\frac{\pi}{4}$ cases. All cases limit to unity in long time.

the alignment time should scale as ξ^{-2}, the experimental results confirm this theory as shown in Figure 9. The high-ξ condition (practically larger than a value of 20) can provide a precise control of the experiments and minimize the control parameters (e.g., ϕ_0). Since $\tau = AB^2t$, at high ξ, where $\Delta\tau$ is a constant, the processing alignment time Δt scales linearly with $1/B^2$. Although the model is based on single-particle dynamics, where the experimental data are collected from very dilute samples (0.001 vol. %), the high-ξ limit also agrees with higher-volume-fraction (0.1 vol. %) samples shown in previous work.[15,26]

Beyond predicting single-particle dynamics, the model developed here can be used as a first-order approximation to predict the probability of alignment in a multi-particle system where particle-particle interaction is negligible. Suppose that the initial orientations of the particles follow a uniform probability distribution on the surface of a unit hemisphere. For a given definition of the alignment time $\Delta\tau$, the probability that the particles are aligned to or beyond the chosen final orientation $p_3^{(2)}$ is

$$\mathbb{P} = \frac{\int_{\phi=0}^{\phi=2\pi}\int_{\theta=0}^{\theta=\arccos p_3^{(1)}} \sin\theta d\theta d\phi}{\int_{\phi=0}^{\phi=2\pi}\int_{\theta=0}^{\theta=\pi/2} \sin\theta d\theta d\phi} = 1 - p_3^{(1)}. \tag{56}$$

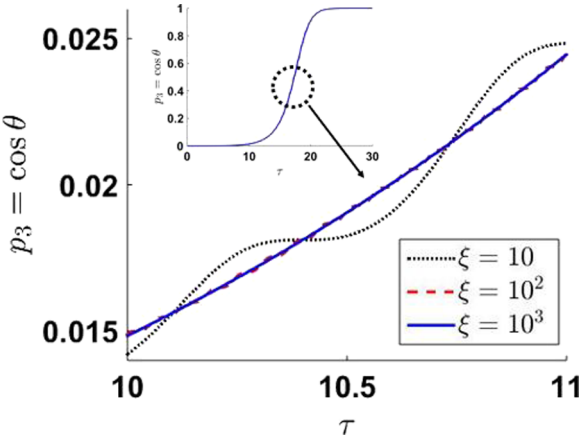

FIG. 8. Evolution of p_3 in rotating field at different $\xi > 1$ with $\phi_0 = 0$. At $\xi = 10$ (the black dotted line), the microdisk wobbles to follow the field. At $\xi = 100$ and $\xi = 1000$ (red dashed and blue solid lines, respectively), the microdisk "sees" the field as a planar field, and the solutions collapse.

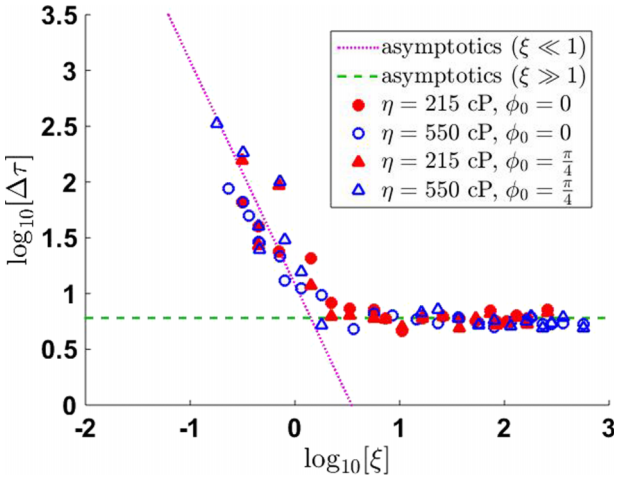

FIG. 9. The alignment time, $\Delta\tau$, chosen from $p_3^{(1)} = 0.1$ to $p_3^{(2)} = 0.9$, versus dimensionless frequency ξ from both the asymptotic solutions and the experiments. At high ξ, the experiments show that the dimensionless alignment time is constant. At low ξ, the dimensionless alignment time grows with decreasing ξ, agreeing with the asymptotic expansion.

Thus, the particles whose initial orientation is smaller than the chosen $p_3^{(1)}$ are not considered to be aligned after $\Delta\tau$.

We believe that variations in the experimental data result from the shape of the particle. In the model, we assumed an axisymmetric disk, but the microdisks produced for this investigated are not perfectly axisymmetric. If distortion from axisymmetry is present, a second axis of orientation exists, and the particle will have a susceptibility to align this second orientation as well. The effect of an extra axis of orientation in the plane is observed in the experiments. After the microdisks are aligned into the field plane, they will continue to wobble in time with the rotating field. Other possible sources of errors come from the assumptions of no random Brownian motion and no translational motion via sedimentation.

V. CONCLUSION

Although the alignment of anisotropic particles has been previously studied experimentally and theoretically, the full analytic solution to predict the orientation of magnetically susceptible microdisks under a rotating magnetic field is presented in this work for the first time. Good agreement with experimental results suggests that the model can be extended to composites with higher volume fraction of particle dispersion and smaller particle size. The model also provides a direction for optimizing the alignment process. In general, by keeping the dimensionless frequency ξ at a high value, the processing alignment time, Δt, can be reduced by increasing the field strength B.

ACKNOWLEDGMENTS

The authors would like to thank Sean Fitzgibbon and Joseph Barakat for their useful discussions and ideas for obtaining the analytic solutions to the differential equations. T.W.W. would like to thank the Medical Research Foundation of Oregon for providing funding.

APPENDIX A: OBLATE SPHEROID RESISTANCE TENSOR

For any resistance tensor, C_{ij}, a corresponding mobility tensor, M_{im}, exists such that $M_{im}C_{ij} = \delta_{jm}$.[29] Multiplying both sides of Eq. (6) by M_{im}, the following expression is obtained for the angular momentum:

$$\omega_m = M_{im}\varepsilon_{ijk}\mu_j B_k - M_{im}\varepsilon_{ijk}p_j\frac{\partial[k_B T \log \Psi]}{\partial p_k}. \tag{A1}$$

Substituting Eq. (A1) into Eq. (7) gives an explicit expression for the orientation rate of change,

$$\frac{dp_\ell}{dt} = M_{im}\varepsilon_{\ell mn}\varepsilon_{ijk}\mu_j B_k p_n - M_{im}\varepsilon_{\ell mn}\varepsilon_{ijk}p_j p_n \frac{\partial k_B T \log \Psi}{\partial p_k}. \tag{A2}$$

If we force the mobility tensor to have the following form

$$M_{im} \equiv C_1\delta_{im} + C_2 p_i p_m, \tag{A3}$$

substitution into Eq. (A2) yields

$$\begin{aligned}\frac{dp_\ell}{dt} &= C_1\varepsilon_{\ell in}\varepsilon_{ijk}\mu_j B_k p_n + C_2\varepsilon_{\ell mn}\varepsilon_{ijk}p_m p_n p_i \mu_j B_k \\ &\quad - C_1\varepsilon_{\ell in}\varepsilon_{ijk}p_j p_n \frac{\partial k_B T \log \Psi}{\partial p_k} - C_2\varepsilon_{\ell mn}\varepsilon_{ijk}p_m p_n p_i p_j \frac{\partial k_B T \log \Psi}{\partial p_k}.\end{aligned} \tag{A4}$$

Since the product of a symmetric tensor and an anti-symmetric tensor is zero, the product $\varepsilon_{\ell mn}p_m p_n$ is null, where $\varepsilon_{\ell mn}$ is anti-symmetric in m and n, while $p_m p_n$ is symmetric in m and n. Thus, the second and fourth terms of Eq. (A4) are zero, and only terms containing C_1 remain. Therefore, only the isotropic term of M_{im}, or equivalently C_{ij}, plays a role in the rotation of an oblate spheroid. We can write

$$C_{ij} = \zeta_r \delta_{ij}, \tag{A5}$$

where ζ_r is equal to $8\pi\eta a^3 Y^C$ from Eq. (8). If the aspect ratio is very large ($\rho \gg 1$), then $Y^C = \frac{4}{3\pi}$, and $C_{ij} = \frac{32\eta a^3}{3}\delta_{ij}$.[29]

APPENDIX B: HIGH PECLÉT LIMIT

Next, we will derive the governing equation by substituting expressions for the induced magnetic dipole Eq. (2), the resistant tensor Eq. (A5), and the angular velocity Eq. (6) into Eq. (A4) to obtain

$$\frac{dp_i}{dt} = -\frac{\left(\chi_\perp^E - \chi_\parallel^E\right)V}{\mu_0\zeta_r} B_n p_n (B_i - B_k p_k p_i) - \frac{k_B T}{\zeta_r}\frac{\partial \log \Psi}{\partial p_i}. \tag{B1}$$

A "rotational Peclét number" is defined such that

$$\begin{aligned}Pe_r &= \frac{\left(\chi_\perp^E - \chi_\parallel^E\right)V B_n p_n (B_i - B_k p_k p_i)}{\mu_0 k_B T} \\ &\sim \frac{\left(\chi_\perp^E - \chi_\parallel^E\right)V B^2}{\mu_0 k_B T}.\end{aligned} \tag{B2}$$

The Peclét number in this study is very high ($O[10^4]$). Thus, the torque caused by Brownian motion can be neglected, and Eq. (B1) becomes Eq. (9).

APPENDIX C: SOLUTION TO ROTATING FIELD

To solve Eq. (25), separating the variables and integrating gives

$$\int \frac{du}{\sin 2u - \xi} = \begin{cases} \dfrac{1}{\sqrt{\xi^2 - 1}} \arctan\left[\dfrac{1 - \xi \tan u}{\sqrt{\xi^2 - 1}}\right], & \text{if} \xi > 1, \\ -\dfrac{1}{\cot u - 1}, & \text{if } \xi = 1, \\ \dfrac{1}{2\sqrt{1 - \xi^2}} \log\left[\dfrac{-\xi \tan u + 1 - \sqrt{1 - \xi^2}}{-\xi \tan u + 1 + \sqrt{1 - \xi^2}}\right], & \text{if } \xi < 1, \end{cases} \tag{C1}$$

which provides the need for separate cases depending on the value of ξ.[32] The solution to Eq. (25) has the form

$$X = D\tau + X_0, \tag{C2}$$

as seen in Eqs. (30), (34), and (38), where D is a constant. Now, Eq. (26) can be integrated such that

$$\begin{aligned} \int \frac{d\theta}{\sin 2\theta} &= -\int \frac{1}{2}\cos^2 u d\tau \quad \text{and} \\ \log[\tan\theta] &= -\int \frac{1}{1+\tan^2 u} d\tau. \end{aligned} \tag{C3}$$

Here $\left[1+\tan^2 u\right]^{-1}$ is used instead of $\cos^2 u$, since Π and K are expressed as $\tan u$, and the integrand in Eq. (C3) can be transformed according to Eq. (28) or Eq. (36).

APPENDIX D: LOW-ξ EXPANSION

The alignment time appears to scale as ξ^{-2} at $\xi \ll 1$. To validate the scaling constant, a Taylor expansion around $\xi = 0$ on the low-ξ solution is necessary. Writing the Taylor expansion around $\xi = 0$ for the Γ-terms gives

$$\Gamma_1 = \left(\lambda_2 - \lambda_1\xi + \frac{1}{4}(3\lambda_2 + \lambda_0)\xi^2 + O\left[\xi^4\right]\right)\exp\left[-\tau\left(\frac{\xi^2}{2} + O\left[\xi^4\right]\right)\right], \tag{D1}$$

$$\Gamma_2 = \left(\lambda_0 - \lambda_1\xi + \frac{1}{4}(\lambda_2 + 3\lambda_0)\xi^2 + O\left[\xi^4\right]\right)\left(1 + \frac{\xi^2\tau}{2} + O\left[\xi^4\right]\right)\exp\left[-2\tau\right], \text{ and} \tag{D2}$$

$$\Gamma_3 = \left(2\lambda_1\xi - (\lambda_0 + \lambda_2)\xi^2 + O\left[\xi^4\right]\right)\exp\left[-\tau\right]. \tag{D3}$$

Because the exponentials in Γ_2 and Γ_3 decay much faster than the exponential decay in Γ_1, the value of Γ_1 is much greater than the values of Γ_2 and Γ_3 when $\tau \gg 1$. Therefore, Eq. (40) can be simplified to be

$$\frac{\tan\theta}{\tan\theta_0} \approx [\Gamma_1]^{1/2}. \tag{D4}$$

Keeping the leading terms in Γ_1 such that $\Gamma_1 \approx \lambda_2 \exp\left[-\frac{\tau\xi^2}{2}\right]$, Eq. (D4) becomes Eq. (47).

[1] V. Imbeni, J. Kruzic, G. Marshall, S. Marshall, and R. Ritchie, "The dentin-enamel junction and the fracture of human teeth," Nat. Mater. **4**, 229–232 (2005).
[2] H. Qi, B. Bruet, J. Palmer, C. Ortiz, and M. Boyce, *Mechanics of Biological Tissue* (Springer, 2005).
[3] W. Yang, I. Chen, B. Gludovatz, E. Zimmermann, R. Ritchie, and M. Meyers, "Natural flexible dermal armor," Adv. Mater. **25**, 31–48 (2013).
[4] J. Vincent and U. Wegst, "Design and mechanical properties of insect cuticle," Arthropod Struct. Dev. **33**, 187–199 (2004).
[5] B. Wilts, H. Whitney, B. Glover, U. Steiner, and S. Vignolini, "Natural helicoidal structures: Morphology, self-assembly and optical properties," Mater. Today Proc. **1**, 177–185 (2014).
[6] R. Erb, R. Libanori, N. Rothfuchs, and A. Studart, "Composites reinforced in three dimensions by using low magnetic fields," Science **335**, 199–204 (2012).
[7] G. Ferk, P. Krajnc, A. Hamler, A. Mertelj, F. Cebollada, M. Drofenik, and D. Lisjak, "Monolithic magneto-optical nanocomposites barium hexaferrite platelets in PMMA," Sci. Rep. **5**, 11395 (2015).
[8] H. Le Ferrand, F. Bouville, T. Niebel, and A. Studart, "Magnetically assisted slip casting of bioinspired hetogeneous composites," Nat. Mater. **14**, 1172–1179 (2015).
[9] R. Erb, J. Segmehl, M. Charilaou, J. F. Loffler, and A. Studart, "Non-linear alignment dynamics in suspensions of platelets under rotating magnetic fields," Soft Matter **8**, 7604–7609 (2012).
[10] F. Bentivegna, M. Nyvlt, J. Ferre, J. Jamet, A. Brun, S. Visnovsky, and R. Urban, "Magnetically textured γ-Fe_2O_3 nanoparticles in a silica gel matrix: Optical and magneto-optical properties," J. Appl. Phys. **85**, 2270–2278 (1999).
[11] M. Liu, Y. Ishida, Y. Ebina, T. Sasaki, T. Hikima, M. Takata, and T. Aida, "An anisotropic hydrogel with electrostatic repulsion between cofacially aligned nanosheets," Nature **517**, 68–72 (2015).
[12] A. Smart, "Stiff yet supple hydrogel mimics cartilage," Phys. Today **68**, 12–14 (2015).
[13] V. Torchilin, "Drug targeting," Eur. J. Pharm. Sci. **11**, S81–S91 (2000).
[14] L. Kong, Z. Liu, L. Liu, R. Huang, M. Abshinova, Z. Yang, C. Tang, P. Tan, C. Deng, and S. Matitsine, "Recent progress in some composite materials and structures for specific electromagnetic applications," Int. Mater. Rev **58**, 203–259 (2013).
[15] H. Song, M. Tan, T. Walker, A. Jander, and P. Dhagat, "Planar alignment of magnetic microdisks in composites using rotating fields," IEEE Trans. Magn. **51**, 1–5 (2015).

[16] R. Han, L. Qiao, T. Wang, and F. Li, "Microwave complex permeability of planar anisotropy carbonyl-iron particles," J. Alloys Compd. **509**, 2734–2737 (2011).
[17] D. Grier, "A revolution in optical manipulation," Nature **424**, 810–816 (2003).
[18] M. Friese, T. Nieminen, N. Heckenberg, and H. Rubinsztein-Dunlop, "Optical alignment and spinning of laser-trapped microscopic particles," Nature **394**, 348–350 (1998).
[19] B. Edwards, T. Mayer, and R. Bhiladvala, "Synchronous electrorotation of nanowires in fluid," Nano. Lett. **6**, 626–632 (2006).
[20] S. Papadakis, Z. Gu, and D. Gracias, "Dielectrophoretic assembly of reversible and irreversible metal nanowire networks and vertically aligned arrays," Appl. Phys. Lett. **88**, 233118 (2006).
[21] P. Smith, C. Nordquist, T. Jackson, T. Mayer, B. Martin, J. Mbindyo, and T. Mallouk, "Electric-field assisted assembly and alignment of metallic nanowires," Appl. Phys. Lett. **77**, 1399 (2000).
[22] L. Sun, K. Keshoju, and H. Xing, "Magnetic field mediated nanowire alignment in liquids for nanocomposite synthesis," Nanotechnology **19**, 405603 (2008).
[23] T. Kimura, M. Yamato, W. Koshimizu, M. Koike, and T. Kawai, "Magnetic orientation of polymer fibers in suspension," Langmuir **16**, 858–861 (2000).
[24] T. Kimura, "Orientation of feeble magnetic particles in dynamic magnetic fields," Jpn. J. Appl. Phys. **48**, 020217 (2009).
[25] M. Sadiku, *Elements of Electromagnetics* (Oxford University Press, 2013).
[26] H. Song, M. Tan, T. Walker, A. Jander, and P. Dhagat, "Planar alignment of isolated magnetic disks in newtonian fluids by a rotating field," IEEE Magn. Lett. **6**, 1 (2015).
[27] B. D. Cullity and C. D. Graham, *Introduction to Magnetic Materials* (IEEE Press, 2009).
[28] S. Kim, "Similarity solutions for the orientation distribution function and rheological properties of suspensions of axisymmetric particles with external couples," J. Non-Newton Fluid Mech. **24**, 297–310 (1987).
[29] S. Kim and S. Karrila, *Microhydrodynamics: Principles and Selected Applications* (Dover, 1991).
[30] J. Happel and H. Brenner, *Low Reynolds Number Hydrodynamics with Special Applications to Particulate Media* (Martinus Nijhoff, 1983).
[31] A. Gast and C. Zukoski, "Electrorheological fluids as colloidal suspensions," Adv. Colloid Interface Sci. **30**, 153–202 (1989).
[32] I. Gradsheteyn and I. Ryzhik, *Table of Integrals, Series, and Products* (Academic Press, 2007).